frontiers | Frontiers in Earth Science

TYPE Original Research
PUBLISHED 06 January 2023
DOI 10.3389/feart.2022.1021308

OPEN ACCESS

EDITED BY
Liguang Wu,
Fudan University, China

REVIEWED BY
Eric Hendricks,
National Center for Atmospheric Research (UCAR), United States
Qingyuan Liu,
Chinese Academy of Meteorological Sciences, China

*CORRESPONDENCE
Yan Li,
yanlee@nuist.edu.cn
Xianyan Chen,
chenxy@cma.gov.cn

SPECIALTY SECTION
This article was submitted to Atmospheric Science, a section of the journal Frontiers in Earth Science

RECEIVED 17 August 2022
ACCEPTED 15 September 2022
PUBLISHED 06 January 2023

CITATION
Jin R, Li Y, Chen X and Li M (2023), Characteristics of the upper-level outflow and its impact on the rapid intensification of Typhoon Roke (2011). *Front. Earth Sci.* 10:1021308. doi: 10.3389/feart.2022.1021308

Characteristics of the upper-level outflow and its impact on the rapid intensification of Typhoon Roke (2011)

Ru Jin[1,2], Yan Li[1]*, Xianyan Chen[3]* and Meiying Li[4]

[1]Key Laboratory of Meteorological Disaster, Ministry of Education (KLME), Nanjing University of Information Science & Technology, Nanjing, China, [2]Zhejiang Institute of Meteorological Sciences, Hangzhou, China, [3]National Climate Center, China Meteorological Administration, Beijing, China, [4]Penglai Meteorological Bureau, Penglai, China

In this study, we investigate the structural characteristics of the upper-level outflow and its impact on the rapid intensification (RI) of Typhoon Roke (2011), which experienced an evident outflow transformation from equatorward to poleward during its RI period. The simulations by the Weather Research and Forecasting Model suggest that the upper-level outflow extends from 100 hPa to 150 hPa, with an upper-level warm core at around 150 hPa. The upper-level outflow is enhanced ahead of the typhoon intensification, which is closely related to the outflow-environment interaction. Further analyses indicate that at the early stage of Roke (2011) before the RI, the strong equatorward outflow and the updraft south of the typhoon center are enhanced, favoring the onset of RI. During the RI period, the strong divergent flow near the entrance of the southwesterly jet in front of the upper-level trough, induces the poleward outflow. The eddy flux convergence of angular momentum inward propagated to the typhoon center from a 1000-km radius further enhances the poleward outflow and leads to the development of the vertical motion north of the typhoon center. Then Roke (2011) intensifies rapidly. Simultaneously, the shallow weak positive potential vorticity (PV) anomaly south of the southwesterly jet increases the inner-core PV, favoring the sustained intensification of Roke (2011). After Roke (2011) reaches its peak intensity, its intensity decreases due to the increase of vertical wind shear and the approaching of the southwesterly jet. It is indicated that the interaction between the upper-level outflow and the upper-tropospheric trough has significant influence on the RI of TC.

KEYWORDS

tropical cyclone, the upper-level outflow, rapid intensification, outflow-environment interaction, upper-troposhere trough

1 Introduction

The characteristics and mechanisms of the intensity variation of tropical cyclones (TCs), especially the rapid intensification (RI), are one of the active areas in TC research (Wang and Zhou, 2008; Zhao et al., 2022a; Cai et al., 2022). Among the several factors affecting TC intensity variation, the upper-level outflow and its interaction with the upper-tropospheric environmental field have attracted more and more attention in recent years (Dai et al., 2017; Ryglicki et al., 2019; Li et al., 2020). The outflow can easily interact with the upper-tropospheric environmental flow due to the weak inertial stability (Holland and Merrill, 1984; Rappin et al., 2011) and the horizontal scale of the outflow can reach thousands of kilometers radially (Ditchek et al., 2017). Simultaneously, the outflow can affect TC intensity through dynamical and thermal processes. Therefore, the study on the characteristics of TC outflow and its influence on the intensity variation can help further understand the mechanisms of TC intensity variation, thus being of great significance to improving TC intensity prediction.

Most TC outflow layers are within 300 hPa to 100 hPa and show anticyclonic and divergent flow on the synoptic scale (Shi et al., 1990). Compared with the middle and lower layers, outflow layers are more asymmetric (Black and Anthes, 1971). Chen and Gray (1985) proposed three outflow patterns for intensifying TCs, namely single channel, double channel and no channel, and the change of outflow patterns is closely related to the upper-tropospheric environmental flow (Merrill, 1988a, b). Recently, with the improvement of detection methods (Komaromi and Doyle, 2017; Ohigashi et al., 2020; Ohigashi et al., 2021) and numerical simulation techniques (Dai et al., 2017; Montgomery et al., 2019), many advances have been achieved in the studies on the characteristics of TC outflow layers and their relationships with TC intensity variation. Using the dropsonde data from the NASA Hurricane and Severe Storm Sentinel (HS3) field campaign, Komaromi and Doyle (2017) found that the outflow extended from 300 hPa to 150 hPa and from 50-km to 200-km radius, with a region of low inertial stability and a shallow inflow layer above the maximum outflow layer. Both model simulations (Cohen et al., 2017) and observations (Cohen et al., 2019) suggested that the outflow layer may exhibit a low-pressure center surrounded by high pressure due to the strong outward-pointing centrifugal and pressure gradient forces that cannot be counterbalanced by the inward-pointing Coriolis force. Furthermore, Cohen and Paldor (2020) analyzed the Lagrangian trajectories of air parcels in the outflow layer and described the dynamics using an integrable, two degrees-of-freedom and angular momentum conserving Hamiltonian system with a single non-dimensional parameter. Several studies focused on the characteristics of low Richardson number in the outflow layer (Emanuel and Rotunno, 2011; Emanuel, 2012; Duran and Molinari, 2016). These studies hypothesized that the critical Richardson number stratifies the potential temperature profile, which leads to the change of outflow temperature with angular momentum to cause the change of TC intensity. However, Montgomery et al. (2019) evaluated the theory of TC intensification proposed by Emanuel (2012) using idealized, three-dimensional, convection-permitting numerical experiments, and the results showed that eddy processes in the outflow layer are more related to TC structure than the critical Richardson number. This finding is consistent with the results in Ditchek et al. (2017) which highlighted the larger dynamic effect of TC outflow layer on TC intensity than the thermodynamic effect.

Generally, TC outflow can influence the TC structure and intensity by interacting with the environmental field (Rappin et al., 2011; Li et al., 2017). Dai et al. (2017) pointed out that the interaction between TC outflow and mid-latitude jets can lead to the formation of the TC secondary eyewall. Moreover, the idealized numerical simulations in Dai et al. (2019) revealed that asymmetric rainbands are an essential source of outflow. However, the scholars are not unanimous on whether the outflow-environment interaction favors TC intensification. Some argued that the strong divergence in front of an upper-level trough, small-scale positive potential vorticity (PV) anomaly and eddy flux convergence (EFC) of angular momentum transported to TC inner-core could enhance TC outflow and develop the secondary circulation, thus intensifying TCs (Molinari and Vollaro, 1989; Hanley et al., 2001; Leroux et al., 2013). Additionally, Ryglicki et al. (2019) found that outflow can divert the environmental flow around TCs, reducing the vertical wind shear (VWS). Therefore, some TCs can still rapidly intensify with moderate VWS (Huang et al., 2022). However, Fischer et al. (2019) investigated the TC-trough interactions for both rapidly and non-rapidly intensifying TCs, and the results revealed that there is little relationship between the RI and EFC. Furthermore, upper-tropospheric systems such as upper-level cold low (UTCL) and mid-latitude jets approaching TCs often result in strong VWS, which can lead to mid-level ventilation, negatively affecting TC intensification (Merrill 1988b; Yan et al., 2021).

However, the mechanism of outflow affecting TC intensity variation is not yet clear. To explore the relationship between the outflow and intensity variation of TCs, we investigate the characteristics of outflow layers during the RI in this study and discuss their possible effects on TC intensity using numerical simulations. The outflow channel of Typhoon Roke (2011) had an evident change during the RI of the TC, which may be related to the outflow-environment interaction. Thus, we select Typhoon Roke (2011) as the study case in this research.

The remainder of this paper is organized as follows. Section 2 presents an overview of Typhoon Roke (2011). Section 3 shows model description and verification. Section 4 describes the characteristics of the upper-level outflow during the RI of Typhoon Roke (2011). Section 5 discusses the possible impacts of the upper-level outflow on the RI of Typhoon

Roke (2011). The main conclusions and discussion are presented in section 6.

2 Overview of Typhoon Roke (2011)

Roke (2011) was a super typhoon with a RI period and a noticeable change in the upper-level outflow channel. According to the best-track dataset from the Joint Typhoon Warning Center (JTWC), Typhoon Roke (2011) started to intensify rapidly at 1800 UTC 18 September and reached its peak at 0000 UTC 20 September, with the maximum wind speed of 59 m s^{-1} and the minimum central pressure of 937 hPa. Then, the RI ended at 0600 UTC 20 September. Based on Wang and Zhou (2008), the criteria for the RI are as follows: the maximum wind speed increases by at least five knots in the first 6 h, 10 knots in the first 12 h and 30 knots in 24 h. The RI period starts when the three criteria are first met simultaneously and ends 24 h later when they are no longer met together (Jiang and Ramirez, 2013).

Mid-to upper-level satellite-derived wind and the water vapor images collected from the Cooperative Institute for Meteorological Satellite Studies (CIMSS) Tropical Cyclones Group at the University of Wisconsin-Madison are used to reveal the evolution of the outflow channel of Typhoon Roke (2011) (Figure 1). 6 h before the onset of RI, there was no apparent outflow channel near the storm center, the cloud system was loose, and a long and narrow jet stream appeared around 10 latitudes north of Roke (2011) (Figure 1A). In the early stage of the RI, the outflow was mainly distributed to the east and south of the upper-level circulation of Roke (2011) (Figure 1B). With the approach of the mid-latitude southwesterly jet, the poleward outflow strengthened, and the equatorward outflow weakened gradually (Figure 1C). Meanwhile, the cloud system of Roke (2011) gradually became dense, and when Roke (2011) reached its peak intensity at 0000 UTC 20 September, the poleward outflow represented by the blue wind barbs was considerably stronger than that in the earlier stage with a mature eyewall in the satellite images (Figure 1D). Therefore, it is evident that the upper-level outflow pattern had a complex transformation with the strengthening of Roke (2011). Furthermore, the RI of Roke (2011) occurred at 26°N–28°N where the sea surface temperature (SST) was relatively low at about 26.5°C–27.5°C. Such an ocean surface cannot provide favorable thermal conditions for the development of Roke (2011). Thus, the leading factor of the intensification of Roke (2011) is the dynamic process of upper-level outflow.

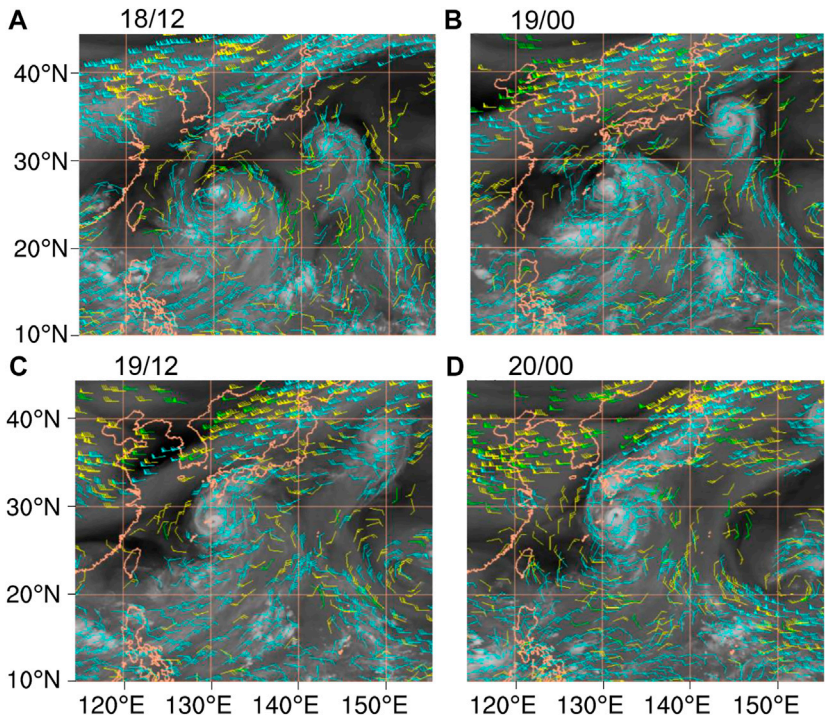

FIGURE 1
Mid-to upper-level satellite-derived wind (green: 351–500 hPa; yellow: 251–350 hPa; blue: 100–250 hPa) superimposed on the water vapor images for Typhoon Roke (2011) at **(A)** 1200 UTC 18 September, **(B)** 0000 UTC 19 September, **(C)** 1200 UTC 19 September and **(D)** 0000 UTC 20 September 2011.

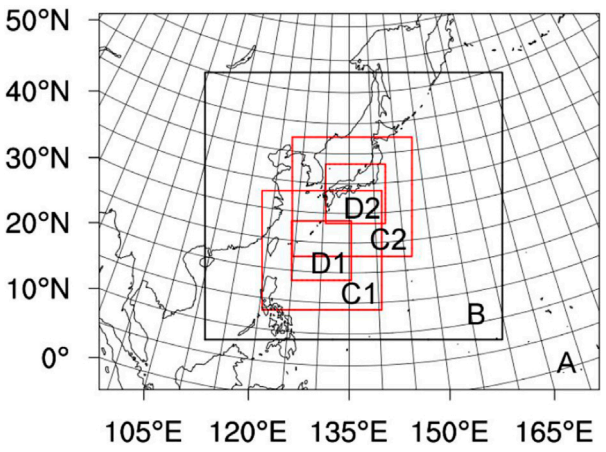

FIGURE 2
Model domain configuration. Domains A, B, C and D have horizontal resolutions of 54, 18, 6 and 2 km, respectively. Domain C and D are designed to follow the movement of the storm, with C1 (D1) and C2 (D2) denoting the initial and final position of the domain, respectively.

3 Model description and verification

3.1 Model description

Considering the limited observation areas of TC outflow and the underestimation of TC intensity in atmospheric reanalysis data (Schenkel and Hart, 2012; Li et al., 2020), the Advanced Research version of the Weather Research and Forecasting Model (WRF-ARW) version 3.4.1 (Skamarock et al., 2008) is used in this study. In this model, we set up four two-way interactive nested domains at horizontal resolutions (grid points) of 54 km (172 × 130), 18 km (307 × 277), 6 km (370 × 370) and 2 km (553 × 553), as shown in Figure 2. The simulations start at 0000 UTC 18 September 2011 and end at 0000 UTC 21 September 2011 in all four domains, with an integration period of 72 h, covering the RI process of Typhoon Roke (2011). The outer domains A and B are stationary, while the inner domains C and D move with the center of Roke (2011) at a 15-min interval, where C1 (D1) and C2 (D2) denote the initial and final positions of the domain C (D), respectively (Figure 2). The outermost domain A is sufficiently large to cover the region of the outflow-environment interaction. In the innermost domain D, the TC inner-core characteristics can be captured at a high resolution. The model initial and lateral boundary conditions in domain A are derived from the interpolation of the National Centers for Environmental Prediction Final Operational Global Analysis (FNL) data, which has spatio-temporal resolutions of 1° × 1° and 6 h. The NCEP FNL analysis is based on the Global Data Assimilation System (GDAS), which continuously collects observational data from the Global Telecommunications System (GTS) and other sources for many analyses. Although the atmospheric motion vectors (AMVs) were not ingested in the NCEP FNL analysis, it is still a good choice to use this data as the initial and boundary conditions in WRF simulations because more other observational data were assimilated into the NCEP FNL analysis. The sea surface temperature data is interpolated from the National Oceanic and Atmospheric Administration's Advanced Very High Resolution Radiometer data with a resolution of 0.25°. The 55 σ-vertical levels are applied in all domains, and the model top is set to 30 hPa (Chen et al., 2011). The vertical resolution is relatively high, especially in both the lower and upper troposphere. For example, there are nine levels from 300 to 100 hPa, all at intervals below 1 km. The time interval of the model outputs is 1 hour.

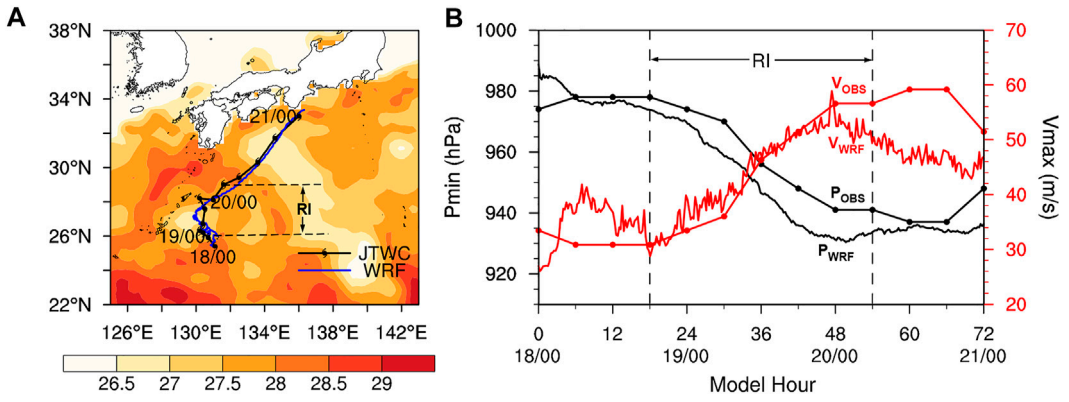

FIGURE 3
(A) Comparison of the track between the observations (black line with typhoon symbols) and simulations (blue line with typhoon symbols) superimposed on the sea surface temperature field (shaded areas, °C) at 0000 UTC 18 September 2011, and **(B)** time series of the maximum surface wind speed (red lines, m s^{-1}) and minimum central pressure (black lines, hPa) of the observations (OBS, dotted lines) and simulations (WRF, solid lines).

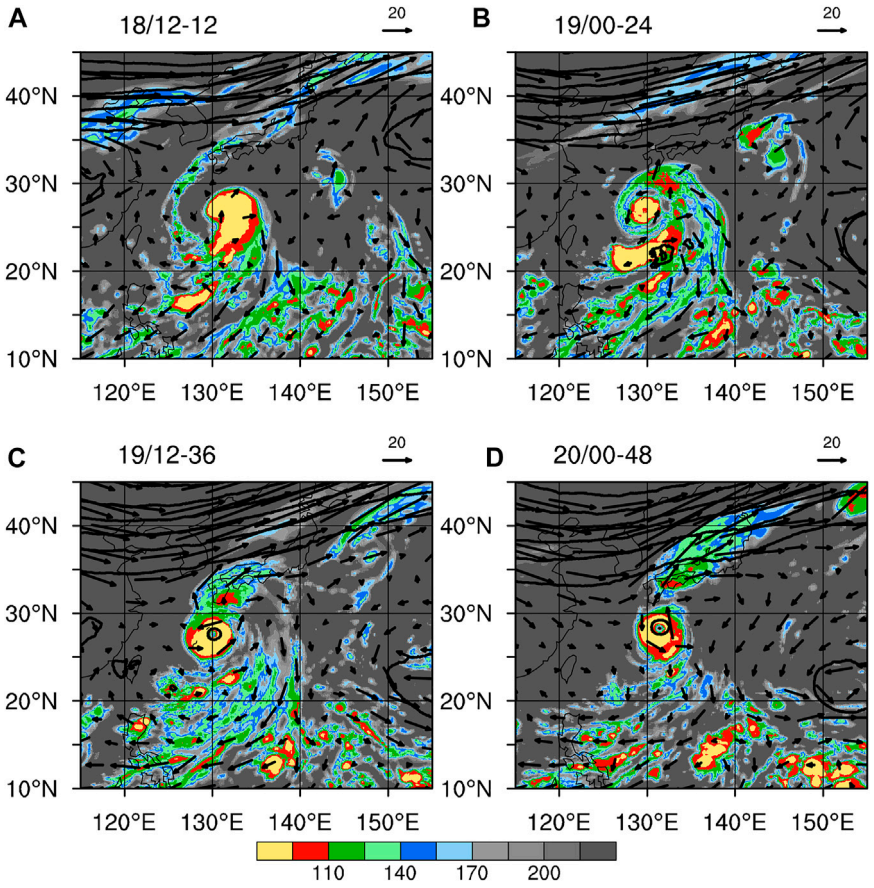

FIGURE 4
The flow (vectors, m s^{-1}), geopotential height (contours, gpm) at 200 hPa and outgoing long-wave radiation (shaded areas, W m^{-2}) for **(A)** 12-h integration (1200 UTC 18 September), **(B)** 24-h integration (0000 UTC 19 September), **(C)** 36-h integration (1200 UTC 19 September) and **(D)** 48-h integration (0000 UTC 20 September).

The physical parameterization schemes used in the model include the Betts-Miller-Janjic cumulus parameterization scheme (Betts, 1986), Yonsei University planetary boundary layer scheme (Hong et al., 2006), unified Noah land surface model scheme (Tewari et al., 2004), Rapid Radiative Transfer Model long-wave radiation scheme (Mlawer et al., 1997), Dudhia shortwave radiation scheme (Dudhia, 1989), and Thompson cloud microphysics scheme including six classes of hydrometeors (Thompson et al., 2004). Note that the Betts-Miller-Janjic cumulus parameterization scheme is only applicable to the domains A and B because it is no need to account for sub-grid-scale convection effects in the domains C and D (Molinari and Dudeck, 1992).

3.2 Model verification

To evaluate the reasonableness of the simulation results, we compare the 72-h simulated track and intensity of Typhoon Roke (2011) with the observations from the JTWC dataset. The results show that the simulated track of Typhoon Roke (2011) is basically consistent with the observations, showing a recurving track from northwestward to northeastward (Figure 3A).

The mean errors of the track in the whole simulation and RI periods are 44.9 km and 54.2 km, respectively. The mean errors of the maximum surface wind speed (V_{MAX}) and the minimum central pressure (P_{MIN}) during the RI period are 3.1 m s^{-1} and 8.5 hPa, respectively (Figure 3B). Therefore, the WRF can simulate well the intensity and RI rate of Typhoon Roke (2011) despite the certain differences in the TC intensity. Specifically, before the onset of RI at 1800 UTC 18 September (0–18 h of integration), the simulated V_{MAX} is obviously stronger than the observations, while the P_{MIN} is closer to the observations. During the RI period from 1800 UTC 18 September to 0000 UTC 20 September (18–48 h of integration), the simulated TC intensity and RI rate are almost the same as the observations. After Roke (2011) reaches its peak intensity at 0000 UTC 20 September, the

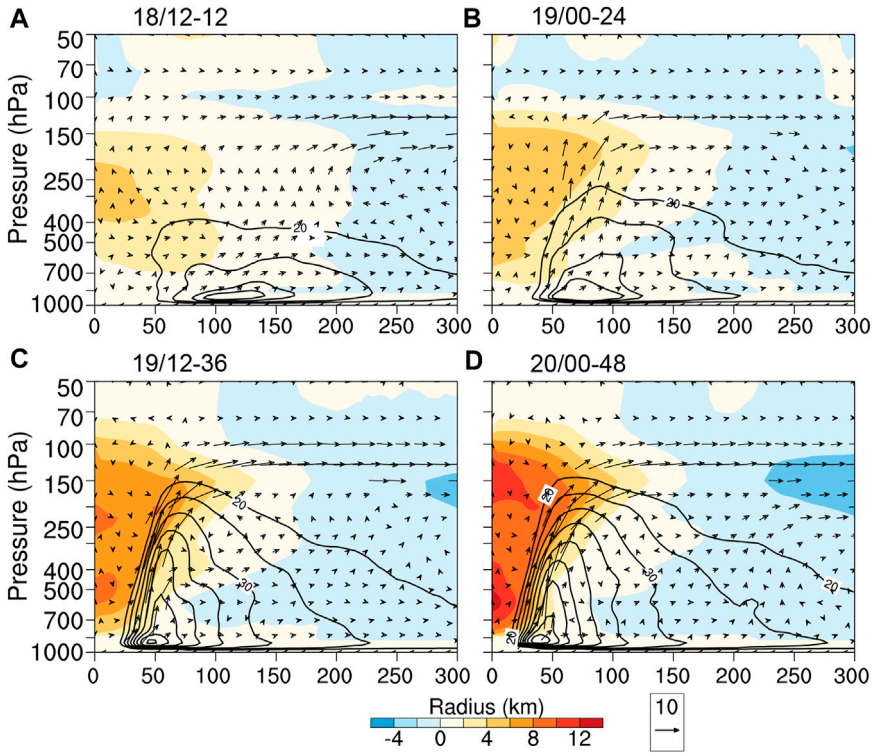

FIGURE 5
Radius-pressure plots of the azimuthally averaged potential temperature anomaly (shaded areas, K), tangential wind (contours, m s^{-1}) and radial-vertical wind velocity (vectors, m s^{-1}; vertical velocity multiplied by 10) for **(A)** 12-h integration (1200 UTC 18 September), **(B)** 24-h integration (0000 UTC 19 September), **(C)** 36-h integration (1200 UTC 19 September) and **(D)** 48-h integration (0000 UTC 20 September).

simulated intensity decreases, which is different from the observed intensity that remained constant and slowly intensified after the end of the RI. Overall, the WRF well simulates the track and intensity variation of Typhoon Roke (2011) during its RI period.

Moreover, the WRF successfully reproduces the upper-tropospheric large-scale environmental field and the upper-level outflow evolution during the intensification of Typhoon Roke (2011) (Figure 4). Specifically, the area of lower outgoing longwave radiation (OLR) which represents the strong convection is mainly distributed south of TC center before the RI (Figure 4A), consistent with the cloud system in Figure 1A. In the early stage of the RI, the low-value OLR area is distributed to the east and south of TC center (Figure 4B), which is similar to that in Figure 1B. In Figures 4C,D, the low-value OLR area north of TC center is greatly expanded, representing the strengthened poleward outflow. Overall, the OLR simulated by the WRF captures the cloud structure well compared with the observations (Figure 1). Simultaneously, the simulated flow and geopotential height fields at 200 hPa exhibit a circulation pattern similar to that in Figure 1. Crucially, the evolution characteristics of the TC outflow are well simulated at higher resolution, providing better conditions for the analyses in the following sections.

4 Characteristics of the upper-level outflow during the rapid intensification of Typhoon Roke (2011)

4.1 Vertical structure of Typhoon Roke (2011)

As shown in Figure 5, the evolution characteristics of the radial and vertical structure during the RI are presented. The warm cores are characterized by the anomalous potential temperature relative to the average temperature in domain D. Six hours before the RI (1200 UTC 18 September), the radius of the maximum tangential wind is around 100 km in the boundary layer, and the outflow appears within 100–200 hPa and at a 200-km radius. Note that the vertical velocity is small, and positive warm anomalies appear between 200 hPa and 400 hPa (Figure 5A). By comparison, the maximum tangential wind is concentrated to inner radius of 75 km, and the outflow markedly intensifies at 125 hPa and 100-km to 250-km radius 6 h after the onset of the RI (0000 UTC 19 September). Simultaneously, the upward motion near the storm center strengthens, and the positive warm anomaly of 4 K extends from 700 hPa to 150 hPa (Figure 5B). With the sustained intensification of

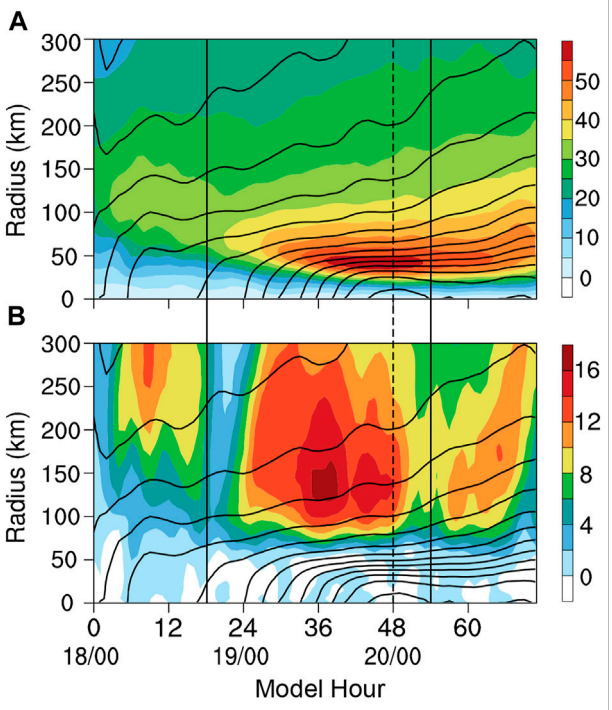

FIGURE 6
Time-radius plots of the azimuthally averaged **(A)** tangential wind (shaded areas, m s^{-1}) at 925 hPa and **(B)** radial wind at 125 hPa (shaded areas, m s^{-1}) and the sea level pressure (contours, hPa). The area between the two solid lines denotes the results in the observed RI period, while the dash lines represent the time when Typhoon Roke (2011) reaches its peak intensity in both simulations and observations.

Roke (2011), the lower-level tangential wind reaches its maximum within a 50-km radius, and the strong outflow peaks at 125 hPa, which can greatly enhance the secondary circulation (Figures 5C,D). Two warm cores arise at 1200 UTC 19 September at around 200 hPa and 500 hPa (Figure 5C), and the upper one peaks at 150 hPa when Roke (2011) reaches its peak intensity at 0000 UTC 20 September (Figure 5D). Overall, it is clear that the outflow is strengthened and thickened during the RI period of Roke (2011).

4.2 Horizontal structure of Typhoon Roke (2011)

Figure 6 presents the time-radius variation of tangential and radial wind with the sea level pressure. The results suggest that the maximum tangential wind at 925 hPa gradually strengthens and approaches the storm center, and then it reaches the peak from 1400 UTC 19 September (38-h integration) to 0400 UTC 20 September (52-h integration). The tangential wind strengthens with the sea level pressure, indicating that the cyclonic rotation increases with decreasing near-surface pressure (Figure 6A). Compared with the tangential wind in the boundary layer, the radial wind representing the wind field of outflow has a larger scale, with four maxima during the simulation (Figure 6B). Before the RI, the first maximum of radial wind speed appears within the radius of 250–300 km, consistent with the finding in Figure 5A. During the RI, the radial wind strengthens gradually and reaches its peak value of more than 16 m s^{-1} at 1200 UTC 19 September (36-h integration) within the radius of 100–150 km. Subsequently, the third maximum of radial speed appears. After the end of the RI, the radial wind strengthens slightly and reaches its fourth maximum. It can be concluded that the variation tendency of radial wind is relatively complex, indicating that the outflow is enhanced before the intensification of the storm, which can provide more favorable conditions for the RI of Roke (2011).

The TC circulation generally shows an asymmetric structure. Figure 7 presents the variation of the upper- and lower-level horizontal structure of Typhoon Roke (2011). Consistent with the results in Cohen et al. (2017, 2019), the 200-hPa wind field is visualized as a small-scale cyclonic flow within a 300-km radius surrounded by a larger-scale anticyclonic flow within an about 1000-km radius (Figures 7A–D). At 1200 UTC 18 September (12-h integration), an upper-level trough with shallow divergent flow appears in the northwest quadrant of the TC center (Figure 7A), where the convective activities are vigorous (Figure 7E). Moreover, the radar reflectivity shows that the asymmetric convection occurs in the east and south of the TC center (Figure 7E), indicating that the primary circulation of Roke (2011) is relatively far away from the upper-level trough. After that, the trough deepens obviously, and the convection is enhanced at 500 km north of the TC center, with the poleward outflow strengthening noticeably (Figure 7B). Simultaneously, the anticyclonic circulation becomes stronger, enhancing the strong convection corresponding to the upper-level outflow at 300 km north of the TC center (Figure 7F). At the following 1200 UTC 19 September and 0000 UTC 20 September, the jet stream and strong divergence in front of the trough approach the TC center gradually (Figures 7C,D), enabling the coupling of the divergent flow at the entrance of the southwesterly jet with the updraft of the TC circulation. Consequently, the poleward outflow is remarkably enhanced with extremely strong convective activities (Figures 7G,H). These analyses indicate that the outflow evolution of Typhoon Roke (2011) is closely related to the upper-tropospheric trough and the southwesterly jet. The dynamic mechanism of the outflow-environment interaction on the intensity variation is further analyzed in the next section.

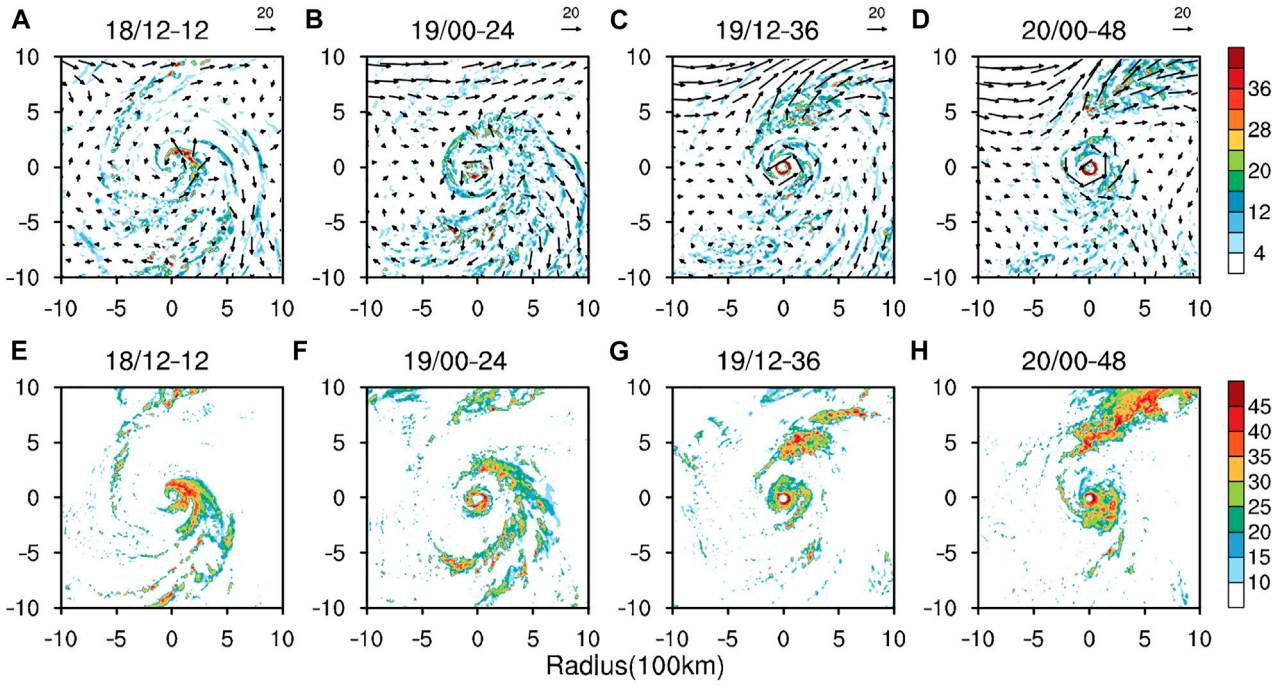

FIGURE 7
(A,B,C,D) The simulated 200-hPa wind field (vectors, m s^{-1}) and divergence (shaded areas, 10^{-5} s^{-1}) and **(E,F,G,H)** the radar reflectivity (dBZ) at 1-km height (around 850 hPa) at **(A,E)** 1200 UTC 18 September (12-h integration) **(B,F)** 0000 UTC 19 September (24-h integration) **(C,G)** 1200 UTC 19 September (36-h integration) and **(D,H)** 0000 UTC 20 September (48-h integration).

5 Impacts of the upper-level outflow on the rapid intensification of Typhoon Roke (2011)

5.1 Upper-tropospheric southwesterly jet and divergence

Typhoon Roke (2011) is a typical case with the outflow-environment interaction during its RI period. Accompanied by the enhancement of the convection and upper-level radial outflow north of the TC center (Figure 7), the sea level pressure decreases, and the surface wind speed increases rapidly (Figure 3). The divergent flow near the entrance of the southwesterly jet is remarkably strong, and the outward mass source needs to be compensated by the upward flow. Therefore, when the outflow and the upward motion are enhanced, the sea level pressure decreases and the TC intensifies. Figure 8 shows that the time-pressure variation of vertical velocity in the south and north of Typhoon Roke (2011) has evident differences because of the upper-level asymmetric structure and the outflow channel transforming from equatorward to poleward. From 1200 UTC 18 September to 0000 UTC 19 September, the relatively strong convection is enhanced within a radius of 400–500 km in the south of the TC center (Figures 7E,F), with strong upward motion in the entire troposphere from 850 hPa to 100 hPa, and then the vertical motion in the south decreases immediately (Figure 8A). Meanwhile, the vertical motion starts to strengthen in TC inner-core region within the radius of 60–80 km (Figure 8C), which indicates the intensification of the TC. The vertical motion in the annulus with a radius of 400–500 km in the north of the TC center gradually strengthens from the upper to lower levels, starting at around 1200 UTC 19 September and peaking at 0000 UTC 20 September (Figure 8B). Therefore, it can be concluded that the strong equatorward outflow enhances the updraft in the south of the TC center, providing favorable conditions for the onset of RI. Moreover, the strong divergence near the entrance of the approaching upper-tropospheric southwesterly jet can strengthen the poleward outflow and drive the strong upward motion in the north of the TC center, favoring the sustained intensification during the RI.

5.2 Eddy flux convergence and vertical wind shear

Several studies have focused on the eddy angular momentum convergence related to the upper-tropospheric synoptic systems,

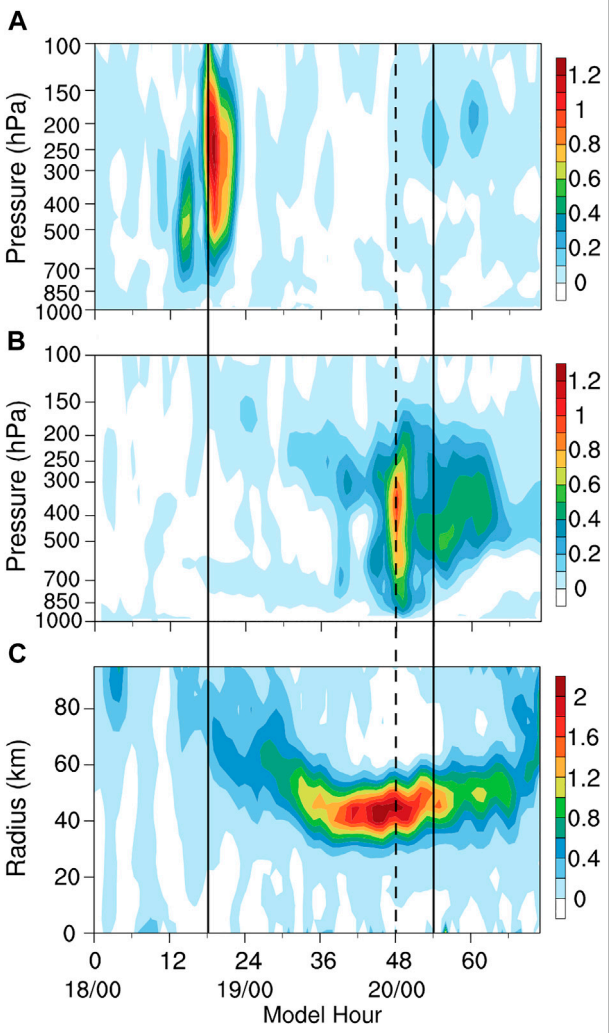

FIGURE 8
Time-pressure plots of the vertical velocity (m s^{-1}) averaged in the annulus with a radius of 400–500 km **(A)** south and **(B)** north of the TC center, and **(C)** the time-radius plot of the azimuthally averaged vertical velocity (m s^{-1}) at 500 hPa. The reference lines represent the same meaning as those in Figure 6.

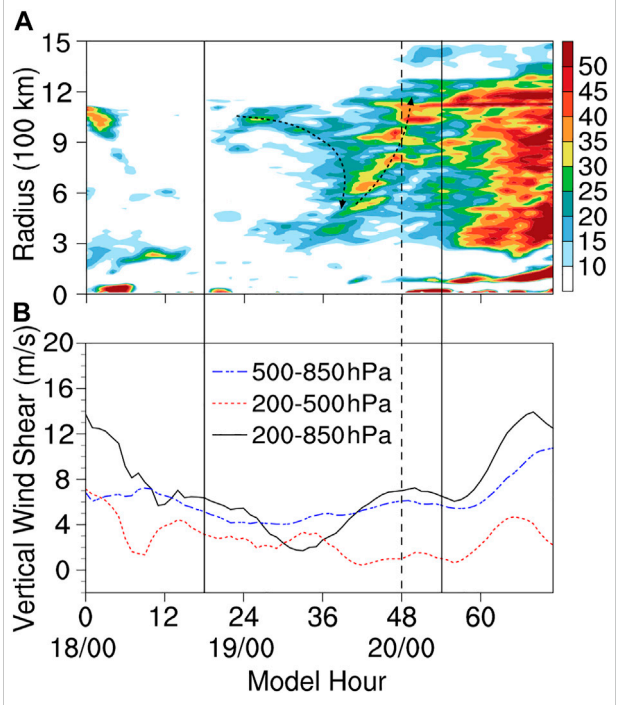

FIGURE 9
(A) The time-radius plot of the azimuthally averaged eddy flux convergence of angular momentum (m s^{-1} day^{-1}) at 200 hPa, and **(B)** time series of the vertical wind shear (m s^{-1}) in the 10° × 10° typhoon-centered region from 200 hPa to 850 hPa (black), 200 hPa to 500 hPa (red) and 500 hPa to 850 hPa (blue). The reference lines represent the same meaning as those in Figure 6.

which can enhance the angular momentum output in TC outflow layers and develop the secondary circulation (Molinari and Vollaro, 1989; Hanley et al., 2001). Therefore, the eddy flux convergence (EFC) of angular momentum can be used as an indicator of the interaction between the TC outflow and the environmental field. The EFC is defined based on Molinari and Vollaro (1989), as shown in Eq. 2.

$$EFC = -\frac{1}{r^2}\frac{\partial}{\partial r}r^2\overline{U'_L V'_L} \quad (2)$$

where r represents the radius from the TC center, U_L denotes the storm-relative radial wind and V_L denotes the storm-relative tangential wind. The overbar represents the azimuthal mean, and the prime denotes the deviation from the azimuthal mean.

As presented in Figure 9A, the temporal evolution of the azimuthally averaged EFC at 200 hPa with the radius from the TC center suggests that the EFC of greater than 10 m s^{-1} day^{-1} (the threshold value of the TC-environment interaction) propagates inward from the area with the 1000-km TC-centered radius, which starts at 0000 UTC19 September (24-h integration), indicating the starting time and location of the TC-environment interaction. Accompanied by the inward propagation of the EFC, the outflow strengthens (Figure 6B) and the upward motion is enhanced (Figure 8C). Moreover, during the RI period of Typhoon Roke (2011), the vertical wind shear (VWS) is relatively weak in different levels, especially in upper levels between 200 hPa and 500 hPa (Figure 9B). Specifically, the 200–850 hPa and 500–850 hPa VWS is less than 8 m s^{-1}, and the 200–500 hPa VWS (mid-to upper levels) is smaller than 4 m s^{-1} during the RI period. According to the result in Ryglicki et al. (2019), the strong divergent outflow can limit the VWS and favor the formation and maintenance of the two warm cores (Figure 5). However, the EFC continuously increases and propagates outward after 1200 UTC on September 19 (36-h integration), indicating the end of the

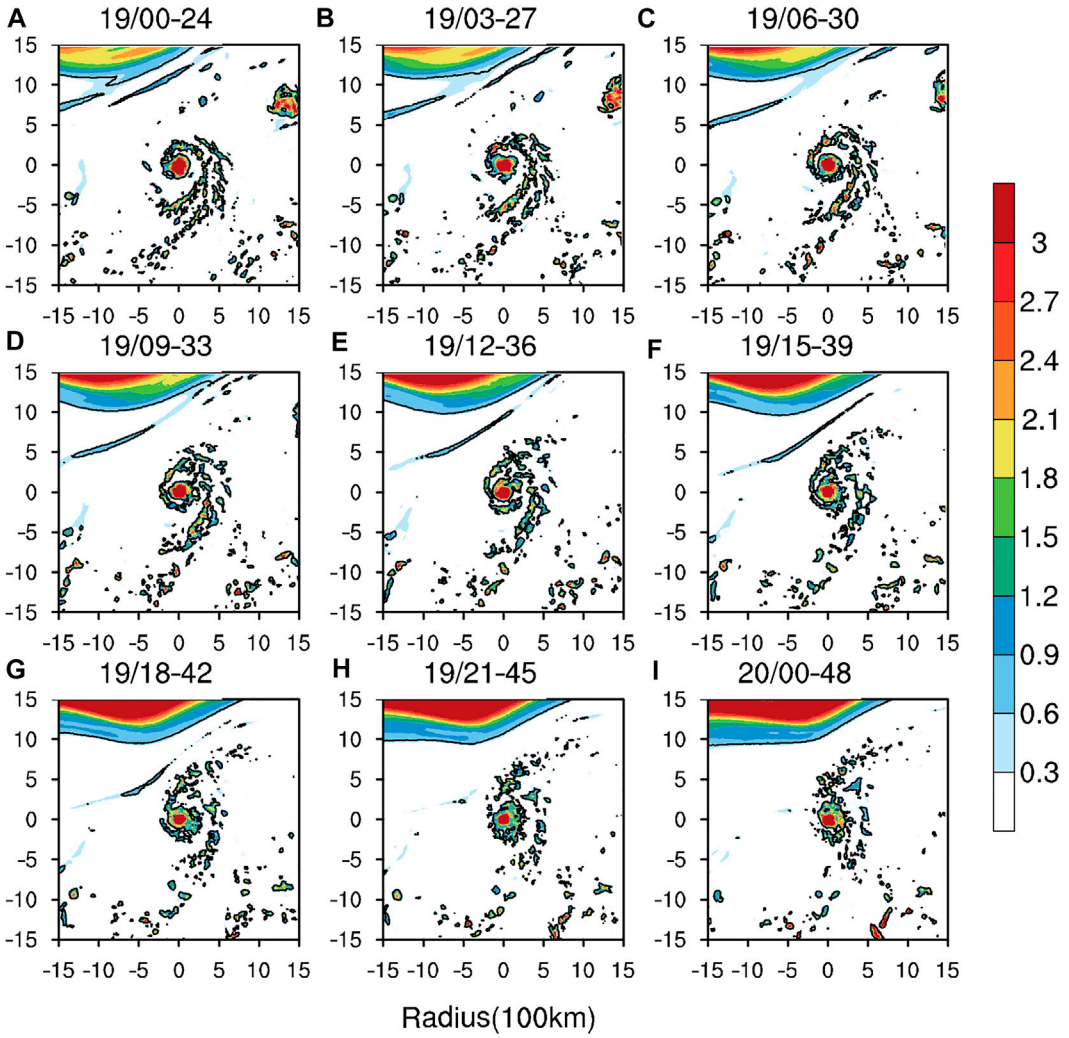

FIGURE 10
The 3-h potential vorticity anomaly (PVU) at the 350-K isentropic surface from 0000 UTC 19 September (24-h integration) to 0000 UTC 20 September (48-h integration). The contour represents the potential vorticity anomaly of 0.3 PVU.

RI. The remarkably enhanced VWS cannot insulate the ventilation influencing the warm cores, inhibiting the strengthening of Roke (2011) after 0600 UTC 20 September (54-h integration).

5.3 Potential vorticity

The PV is a comprehensive physical quantity which contains the information of both thermodynamic and dynamic states of the atmosphere. Unlike absolute vorticity, the PV is conserved in adiabatic frictionless flow. Thus, the evolution of the atmospheric perturbations can be traced by the PV anomaly (Hoskins et al., 1985). Numerous studies have used the Ertel PV to investigate the interaction between the TCs and upper-tropospheric circulation systems (Molinari and Vollaro, 1989; Molinari and Vollaro, 1989; Leroux et al., 2013; Perez-Reyes, 2016). The Ertel PV is defined as follows (Eq. 1)

$$PV = (f + \zeta_\theta)\left(-g\frac{\partial\theta}{\partial p}\right) \quad (1)$$

where and represent the absolute vorticity and the static stability on the isentropic surface, respectively. The unit of the Ertel PV is PVU (1 PVU = 10^{-6} m^2 K s^{-1} kg^{-1}).

Figure 10 presents the 3-h distribution and variation of the simulated PV anomaly in domain B at the 350-K isentropic surface (between 175 hPa and 225 hPa). The results indicate that the positive PV anomaly is mainly distributed around the TC center and the upper-tropospheric southwesterly jet area, where the perturbations are relatively strong. From 0000 UTC 19 September (24-h integration)

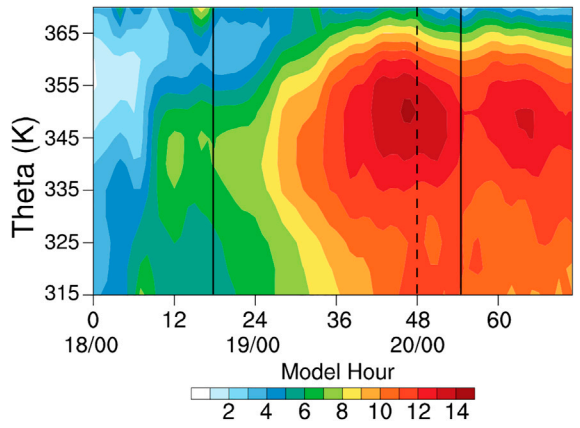

FIGURE 11
The time-theta plot of the potential vorticity (PVU) with isentropic surfaces in the 100 km × 100 km typhoon-centered region. The reference lines represent the same meaning as those in Figure 6.

to 1800 UTC 19 September (42-h integration), the shallow weak positive PV anomaly separated from south of the southwesterly jet gradually approaches the TC center, and the large-scale positive PV anomaly north of the TC center rises simultaneously. In the inner-core region, the PV increases from upper levels between 345-K and 355-K isentropic surfaces, transfers downward to lower levels and peaks at 0000 UTC 20 September (48-h integration), as shown in Figure 11. This result is consistent with the development of TC intensity. Therefore, the approaching southwesterly jet favors the enhancement and downward transmission of the upper-level positive PV, and it can increase the distance of isentropic surfaces in lower levels and decrease the atmospheric static stability (Hoskins et al., 1985). Due to the conservation property of PV on isentropic surfaces, the cyclonic vorticity in lower levels increases and the TC intensifies (Leroux et al., 2013).

6 Conclusion and discussion

Recently, the upper-level outflow has been recognized as an essential factor influencing TC intensification (Dai et al., 2017; Ryglicki et al., 2019; Li et al., 2020), but it remains a challenge to interpret the mechanism of its influence on TC intensity. In this study, Typhoon Roke (2011), with a clear outflow channel transformation from equatorward to poleward, is chosen to investigate this question. The results suggest that the track and intensity of Typhoon Roke (2011) during the RI period can be well reproduced by the WRF-ARW version 3.4.1. The high-resolution simulations for Typhoon Roke (2011) show the structure characteristics of the upper-level outflow and its impact on the RI of Roke (2011).

The upper-level characteristics of Typhoon Roke (2011) during the RI are as follows. The upper-level outflow expands from 100 hPa to 150 hPa, and constitutes the secondary circulation of the TC with an ascending branch of the vertical motion. Two warm cores are formed with the intensification of Typhoon Roke (2011), and the upper one appears at around 150 hPa. The upper-level outflow is enhanced ahead of the TC intensification, which is closely related to the upper-tropospheric trough and the southwesterly jet.

Further analyses indicate the possible impact of the outflow on the RI of Typhoon Roke (2011). Before the RI, the strong equatorward outflow and the upward motion are enhanced south of the TC center, favoring the onset of RI at the early stage of Roke (2011). During the RI period, there is strong divergent flow near the entrance of the southwesterly jet, and the EFC propagates inward from the area with the 1000-km typhoon-centered radius, enhancing the poleward outflow of Roke (2011). Moreover, the strong divergent flow restricts the VWS, protecting the warm cores from the ventilation. In this circulation situation, the updraft in the north of the TC center develops and Roke (2011) intensifies rapidly. Simultaneously, the shallow weak positive PV anomaly south of the southwesterly jet approaches the TC center, and the inner-core PV increases, favoring the sustained intensification of Roke (2011).

Unlike the results in previous studies focusing on the TC-environment interaction before the TC intensification (Molinari and Vollaro, 1989; Leroux et al., 2013), Typhoon Roke (2011) underwent the interaction of outflow and the southwesterly jet after the RI starts, which was conducive to the maintenance but not the onset of RI. The equatorward outflow enhanced at the earlier stage is probably due to the Fujiwara effect proposed in Sonca (2011) or the equatorial flow, which is to be demonstrated in future work.

In this research, the diagnostic analysis is carried out based on the simulations from the control experiment, and no sensitivity experiment is designed to confirm the impact of the upper-level outflow on the TC intensity. In the future, the sensitivity experiments will be conducted, such as changing the intensity of the upper-tropospheric synoptic systems and their distance from the TC, to explore and verify the mechanism of the outflow-environment interaction on TC intensity.

Data availability statement

The original contributions presented in the study are included in the article/supplementary material, further inquiries can be directed to the corresponding authors.

Author contributions

YL and XC designed research. RJ conceptualized the analysis and wrote the manuscript. All authors were

involved in helpful discussions and contributions to the manuscript.

Funding

This work was jointly supported by National Key Research and Development Program of China (2017YFA0605004), and the National Natural Science Foundation of China (41775058). We acknowledge the High Performance Computing Center of Nanjing University of information science and technology for their support of this work.

The authors declare that this study received funding from the project of China Three Gorges Corporation (0704182). The funder was not involved in the study design, collection, analysis, interpretation of data, the writing of this article, or the decision to submit it for publication.

Conflict of interest

The authors declare that the research was conducted in the absence of any commercial or financial relationships that could be construed as a potential conflict of interest.

Publisher's note

References

Betts, A. K. (1986). A new convective adjustment scheme. Part I: Observational and theoretical basis. *Q. J. R. Meteorol. Soc.* 112, 677–691. doi:10.1002/qj.49711247307

Black, P. G., and Anthes, R. A. (1971). On the asymmetric structure of the tropical cyclone outflow layer. *J. Atmos. Sci.* 28, 1348–1366. doi:10.1175/1520-0469(1971)028<1348:otasot>2.0.co;2

Cai, Y., Han, X., Zhao, H., Klotzbach, P. J., Wu, L., Raga, G. B., et al. (2022). Enhanced predictability of rapidly intensifying tropical cyclones over the Western North Pacific associated with snow depth changes over the Tibetan Plateau. *J. Clim.* 35, 2093–2110. doi:10.1175/JCLI-D-21-0758.1

Chen, H., Zhang, D. L., Carton, J., and Atlas, R. (2011). On the rapid intensification of hurricane wilma (2005). Part I: Model prediction and structural changes. *Wea. Forecast.* 26, 885–901. doi:10.1175/WAF-D-11-00001.1

Chen, L. S., and Gray, W. M. (1985). Global view of the upper level outflow pattern associated with tropical cyclone intensity changes during FGGE. *Dept. Atmos. Sci. Pap.* 392, 126.

Cohen, Y., Durden, S. L., Harnik, N., and Heifetz, E. (2019). Relating observations of gradient non balance at the top of hurricanes with their warm core structures. *Geophys. Res. Lett.* 46, 11510–11519. doi:10.1029/2019GL084248

Cohen, Y., Harnik, N., Heifetz, E., Nolan, D. S., Tao, D., and Zhang, F. (2017). On the violation of gradient wind balance at the top of tropical cyclones. *Geophys. Res. Lett.* 44, 8017–8026. doi:10.1002/2017GL074552

Cohen, Y., and Paldor, N. (2020). Lagrangian trajectories at the outflow of tropical cyclones. *Q. J. R. Meteorol. Soc.* 147, 58–73. doi:10.1002/qj.3904

Dai, Y., Majumdar, S. J., and Nolan, D. S. (2017). Secondary eyewall formation in tropical cyclones by outflow-jet-interaction. *J. Atmos. Sci.* 74, 1941–1958. doi:10.1175/JAS-D-16-0322.1

Dai, Y., Majumdar, S. J., and Nolan, D. S. (2019). The outflow–rainband relationship induced by environmental flow around tropical cyclones. *J. Atmos. Sci.* 76, 1845–1863. doi:10.1175/JAS-D-18-0208.1

Ditchek, S. D., Molinari, J., and Vollaro, D. (2017). Tropical cyclone outflow-layer structure and balanced response to eddy forcings. *J. Atmos. Sci.* 74, 133–149. doi:10.1175/JAS-D-16-0117.1

Dudhia, J. (1989). Numerical study of convection observed during the winter monsoon experiment using a mesoscale two-dimensional model. *J. Atmos. Sci.* 46, 3077–3107. doi:10.1175/1520-0469(1989)046<3077:nsocod>2.0.co;2

Duran, P., and Molinari, J. (2016). Upper-tropospheric low richardson number in tropical cyclones: Sensitivity to cyclone intensity and the diurnal cycle. *J. Atmos. Sci.* 73, 545–554. doi:10.1175/JAS-D-15-0118.1

Emanuel, K., and Rotunno, R. (2011). Self-stratification of tropical cyclone outflow. Part I: Implications for storm structure. *J. Atmos. Sci.* 68, 2236–2249. doi:10.1175/JAS-D-10-05024.1

Emanuel, K. (2012). Self-stratification of tropical cyclone outflow. Part II: Implications for storm intensification. *J. Atmos. Sci.* 68, 988–996. doi:10.1175/JAS-D-11-0177.1

Fischer, M. S., Tang, B. H., and Corbosiero, K. L. (2019). A climatological analysis of tropical cyclone rapid intensification in environments of upper-tropospheric troughs. *Mon. Weather Rev.* 147, 3693–3719. doi:10.1175/MWR-D-19-0013.1

Hanley, D., Molinari, J., and Keyser, D. (2001). A composite study of the interactions between tropical cyclones and upper-tropospheric troughs. *Mon. Weather Rev.* 129, 2570–2584. doi:10.1175/1520-0493(2001)129<2570:acsoti>2.0.co;2

Holland, G., and Merrill, R. T. (1984). On the dynamics of tropical cyclone structural changes. *Q. J. R. Meteorol. Soc.* 110, 723–745. doi:10.1002/qj.49711046510

Hong, S. Y., Noh, Y., and Dudhia, J. (2006). A new vertical diffusion package with an explicit treatment of entrainment processes. *Mon. Weather Rev.* 134, 2318–2341. doi:10.1175/MWR3199.1

Hoskins, B. J., Mcintyre, M. E., and Robertson, A. W. (1985). On the use and significance of isentropic potential vorticity maps. *Q. J. R. Meteorol. Soc.* 111, 877–946. doi:10.1002/qj.49711147002

Huang, Q., Ge, X., and Bi, M. (2022). Simulation of rapid intensification of super typhoon Lekima (2019). Part II: The critical role of cloud-radiation interaction of asymmetric convection. *Front. Earth Sci.* 9, 1–14. doi:10.3389/feart.2021.832670

Jiang, H., and Ramirez, E. M. (2013). Necessary conditions for tropical cyclone rapid intensification as derived from 11 years of TRMM Data. *J. Clim.* 26, 6459–6470. doi:10.1175/JCLI-D-12-00432.1

Komaromi, W. A., and Doyle, J. D. (2017). Tropical cyclone outflow and warm core structure as revealed by HS3 dropsonde data. *Mon. Weather Rev.* 145, 1339–1359. doi:10.1175/MWR-D-16-0172.1

Leroux, M. D., Plu, M., Barbary, D., Roux, F., and Arbogast, P. (2013). Dynamical and physical processes leading to tropical cyclone intensification under upper-level trough forcing. *J. Atmos. Sci.* 70, 2547–2565. doi:10.1175/JAS-D-12-0293.1

Li, Y., Jin, R., and Gao, X. (2020). Outflow-jet interaction analysis of tropical cyclone Roke (2011) within different atmospheric reanalysis datasets. *Trans. Atmos. Sci.* 43, 525–536. (in Chinese). doi:10.13878/j.cnki.dqkxxb.20180302001

Li, Y., Zhou, H., Ge, X. Y., and Jin, R. (2017). Characteristics of the outflow layer of tropical cyclone rapid intensification in the Western North Pacific. *J. Trop. Meteor.* 33, 145–154. (in Chinese). doi:10.16032/j.issn.1004-4965.2017.02.001

Merrill, R. T. (1988a). Characteristics of the upper-tropospheric environmental flow around hurricanes. *J. Atmos. Sci.* 45, 1665–1677. doi:10.1175/1520-0469(1988)045<1665:cotute>2.0.co;2

Merrill, R. T. (1988b). Environmental influences on hurricane intensification. *J. Atmos. Sci.* 45, 1678–1687. doi:10.1175/1520-0469(1988)045<1678:eiohi>2.0.CO;2

Mlawer, E. J., Taubman, S. J., Brown, P. D., Iacono, M. J., and Clough, S. A. (1997). Radiative transfer for inhomogeneous atmospheres: RRTM, a

validated correlated-k model for the longwave. *J. Geophys. Res.* 102, 16663–16682. doi:10.1029/97JD00237

Molinari, J., and Dudeck, M. (1992). Parameterization of convective precipitation in mesoscale numerical models: A critical review. *Mon. Wea. Rev.* 120, 326–344. doi:10.1175/1520-0493(1992)120<0326:pocpim>2.0.co;2

Molinari, J., and Vollaro, D. (1989). External influences on hurricane intensity. Part I: Outflow layer eddy angular momentum fluxes. *J. Atmos. Sci.* 46, 1093–1105. doi:10.1175/1520-0469(1989)046<1093:eiohip>2.0.co;2

Montgomery, M. T., Persing, J., and Smith, R. K. (2019). On the hypothesized outflow control of tropical cyclone intensification. *Q. J. R. Meteorol. Soc.* 145, 1309–1322. doi:10.1002/qj.3479

Rappin, E. D., Morgan, M. C., and Tripoli, G. J. (2011). The impact of outflow environment on tropical cyclone intensification and structure. *J. Atmos. Sci.* 68, 177–194. doi:10.1175/2009JAS2970.1

Ryglicki, D. R., Doyle, J. D., Hodyss, D., Cossuth, J. H., Jin, Y., Viner, K. C., et al. (2019). The unexpected rapid intensification of tropical cyclones in moderate vertical wind shear. Part III: Outflow-environment interaction. *Mon. Weather Rev.* 147, 2919–2940. doi:10.1175/MWR-D-18-0370.1

Schenkel, B. A., and Hart, R. E. (2012). An examination of tropical cyclone position, intensity, and intensity life cycle within atmospheric reanalysis datasets. *J. Clim.* 25, 3453–3475. doi:10.1175/2011JCLI4208.1

Shi, J. J., Chang, S. W. J., and Raman, S. (1990). A numerical study of the outflow layer of tropical cyclones. *Mon. Wea. Rev.* 118, 2042–2055. doi:10.1175/1520-0493(1990)118<2042:ansoto>2.0.CO;2

Skamarock, W. C., Klemp, J. B., Dudhia, J., David, O. G., and Jordan, G. P. (2008). *A description of the advanced research WRF version 3*. Boulder: NCAR Tech. Note NCAR/TN-475+STR. doi:10.5065/D68S4MVH

Tewari, M. F., Chen, W., Wang, J., Dudhia, M. A., LeMone, K., Mitchell, M., et al. (2004). "Implementation and verification of the unified Noah land surface model in the WRF model," in 20th Conf. on Weather Analysis and Forecasting/16th Conf. on Numerical Weather Prediction, Washington, 14 January, 2004 (Seattle, WA: Amer. Meteor. Soc.). Available at: https://ams.confex.com/ams/pdfpapers/69061.pdf.

Wang, B., and Zhou, X. (2008). Climate variation and prediction of rapid intensification in tropical cyclones in the Western North Pacific. *Meteorol. Atmos. Phys.* 99, 1–16. doi:10.1007/s00703-006-0238-z

Yan, Z., Ge, X., Wang, Z., Wu, C., and Peng, M. (2021). Understanding the impacts of upper-tropospheric cold low on typhoon Jongdari (2018) using piecewise potential vorticity inversion. *Mon. Weather Rev.* 149, 1499–1515. doi:10.1175/MWR-D-20-0271.1

Zhao, H., Zhao, K., Klotzbach, P. J., Wu, L., and Wang, C. (2022a). Interannual and interdecadal drivers of meridional migration of western north pacific tropical cyclone lifetime maximum intensity location. *J. Clim.* 35, 2709–2722. doi:10.1175/JCLI-D-21-0797.1